Automated Aerial Screwing with a Fully Actuated Aerial Manipulator

Schuster, Micha; Bernstein, David; Reck, Paul; Hamaza, S.; Beitelschmidt, Michael

DOI
10.1109/IROS47612.2022.9981979

Publication date
2022

Document Version
Final published version

Published in
IEEE/RSJ International Conference on Intelligent Robots and Systems, IROS 2022

2022 IEEE/RSJ International Conference on Intelligent Robots and Systems (IROS)
October 23-27, 2022, Kyoto, Japan

Automated Aerial Screwing with a Fully Actuated Aerial Manipulator

Micha Schuster[1], David Bernstein[1], Paul Reck[1], Salua Hamaza[2] and Michael Beitelschmidt[1]

Abstract— **The tasks that unmanned aerial vehicles (UAVs) have taken upon have progressively grown in complexity over the years, alongside with the level of autonomy with which they are carried out. In this work, we present an example of aerial screwing operations with a fully-actuated tilt-rotor platform. Key contributions include a new control framework to automate screwing operations through a robust hole search and in-hole detection algorithm. These are achieved without a-priori knowledge of the exact hole location, and without the use of external tools, such as vision based hole detection or force sensors. Wrench coupling is implemented to account for the platform's kinematic constraints during screwing. The application of a constant contact force and a compliant response to induced disturbances are obtained with the use of admittance control. The full framework is validated with extensive flight experiments that demonstrate the effectiveness of each subsystem, as well as the complete architecture. We also validate the robustness of the detection algorithm against false positives. Within the results we demonstrate the ability to perform the automated task with a 86% success rate over 35 flights, and measured hole search time of 9s (median value).**

I. Introduction

In the last decades, underactuated unmanned aerial vehicles (UAVs) have mainly been used as sensing platforms, especially for applications in visual inspection, monitoring and mapping. The research field in *aerial manipulation* greatly expands upon aerial robots' capabilities and reach, by demonstrating their use for interaction tasks with the surroundings. Example applications include grasping, load transportation, peg-in-hole, aerial writing, and the exertion of force against different targets and surfaces for use cases like none destructive testing, sensor placement, human-aided drilling and screwing [1]–[6]. Thanks to their vertical take-off and landing (VTOL) abilities, agility and accessibility, they have become suitable candidates for servicing and maintaining infrastructure, offsetting the risks involved with such operations carried out by humans at height [7]–[9]. Most contact-based applications demand different behaviours of the UAV during the free flight and the contact phases. Three main aspects are associated with aerial interaction tasks, namely force control, motion planning and target detection. The state-of-the-art shows examples of different controllers used, in combination with different perception methods to aid the autonomy aspect. With regards to interaction controllers implemented for aerial manipulation, two main approaches are found: direct and indirect methods.

[1]Micha Schuster, David Bernstein, Paul Reck and Michael Beitelschmidt are with the Chair for Dynamics and Mechanism Design, Technische Universität Dresden (TU Dresden), Dresden, Germany. Email: micha.schuster@tu-dresden.de

[2]Salua Hamaza is with the Micro Air Vehicle Laboratory, Delft University of Technology (TU Delft), Delft, The Netherlands.

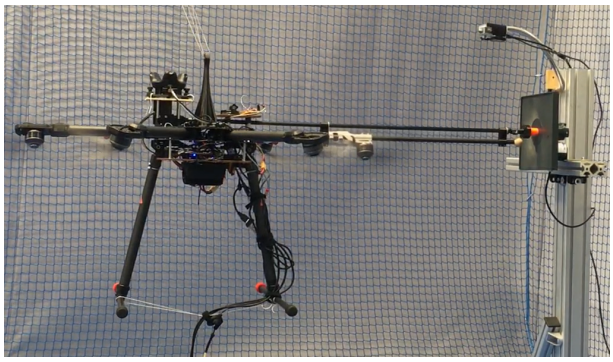

Fig. 1: Aerial screwing with a fully-actuated UAV.

Indirect methods are widely used to generate a compliant behavior in response to external forces with impedance or admittance control schemes [1], [4], [10]. Other works make use of direct force control by adopting onboard force and torque sensing, in a closed-loop fashion [11], [12]. With regards to motion planning and trajectory generation, three approaches are found to render autonomy: when the system is manually operated by a pilot and therefore no trajectory is defined (no autonomy) [13], when a Motion Capture System (MoCap) is used to determine the target pose in real-time (low autonomy) and compute the trajectory [1], and when the trajectory generation is fully based on visual feedback that estimates the target pose (high autonomy) as in [6]. Lastly, as different control envelopes are used for contact and free flight, the transition between them is either appointed to a human operator as seen in [6], [13], or autonomously achieved via onboard force sensing and state estimation [11], [12].

Based on the above efforts, this work presents a novel approach to aerial screwing using a fully-actuated UAV with fixed tilted rotors. To achieve this, we develop a detailed cascade control architecture that addresses various nuances involved in the screwing process. This enables to have a higher autonomy in delivering aerial screwing without the use of external tools, such as vision based hole detection or force sensors. As part of our proposed strategy we implement an admittance controller to adjust the vehicle's position during the contact phase, and render a continuous force during the screwing operation while maintaining the vehicle's stability. Within the scope of the paper, autonomous detection of the hole in the target area and a robust response to false positives are part of the key results; while motion planning prior to the screwing task is not hereby considered. The contributions of this work can be then summarized:

- We present an aerial manipulator system, capable of

2022 IEEE/RSJ International Conference on Intelligent Robots and Systems (IROS) | 978-1-6654-7927-1/22/$31.00 ©2022 IEEE | DOI: 10.1109/IROS47612.2022.9981979

screwing into vertical walls indoors with a success rate of 86% out of 35 flights without vision or force sensors.
- We propose a technique to autonomously find the target hole without any a-priori knowledge of the exact hole location.
- We propose a control strategy that is robust against the UAV's reduced degree of freedom during the screwing process.
- We exploit the inherent capabilities of fully actuated UAVs in force generation to strengthen the robustness of aerial screwing.

II. Problem Statement

As we focus on the screwing process, we assume the hole to be present on the target surface beforehand. The aerial screwing process can be divided into several phases, or sub-tasks. Prior to and after the screwing task, the UAV is hovering in free-flight. For the operational phases in between, we define the following constraints and assumptions:

1) **Target Surface Localization**
   We assume the target area to be a vertical flat surface of which position and orientation are known a-priori, and that we can approach the surface perpendicularly. However, the hole location is only known within an area of several centimeters on the target surface.
2) **Transition from Free Flight to Contact Flight**
   The UAV is approaching the target surface until the screw tip is in contact to the target surface. When contact is detected, a contact force is generated to ensure continuous contact.
3) **Screw-Target Interface**
   We assume the surface texture in the surrounding area of the hole to be smooth enough to allow a lateral sliding of the screw tip. We also assume the screw to have a flat tip, e.g. similar to a bolt, to allow sliding motion over the target surface.
4) **Hole Detection and Screw Insertion**
   In some rare occurances, the screw might enter the hole directly at first contact. In most cases, the hole is unlikely to be found at the first hit. Hence, the screw will be moved over the target surface until the screw tip enters the hole, which is essentially a combination of a push-and-slide and a peg-in-hole task. This increases the robustness and repeatability of the process, as the information on the exact hole location is not necessary. When the screw tip enters the hole, lateral movements of the screw tip are no longer possible due to the mechanical coupling. This translates to lower degrees of freedom (DOF) in the system as a whole. The screw is rotated until it is completely screwed in and a desired tightening torque is reached.
5) **Undocking and Transition into Free Flight**
   To undock the UAV from the screw, a force vector pointing away from the target surface is generated by the force controller until the UAV returns to free flight.

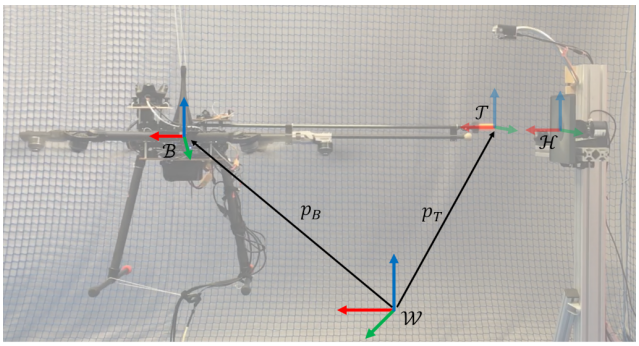

Fig. 2: Aerial manipulator with used reference frames. The axis colors are: x-red, y-green, z-blue.

III. System Design and Modelling

The system consists of a fully actuated UAV and a 1 DOF manipulator for screwing. The fixed world frame is denoted with $\mathcal{W}$; the body-fixed frame $\mathcal{B}$ lies in the center of the UAV; frame $\mathcal{T}$ is centred in the tool center point (TCP), i.e. the screw tip; and the target resp. hole frame $\mathcal{H}$ is located at the center of the search area on the target surface, as depicted in Fig. 2. If not explicitly specified differently, all translational quantities (position $\boldsymbol{p}$, force $\boldsymbol{f}$, etc.) are expressed w.r.t. the world frame $\mathcal{W}$, all rotational quantities (angular velocity $\boldsymbol{\omega}$, inertia tensor Θ, torque $\boldsymbol{\tau}$ etc.) are expressed w.r.t. the body fixed frame $\mathcal{B}$.

A. Aerial Vehicle

The UAV of mass m is a fully actuated hexacopter with fixed tilted rotors. The simplified dynamic model of the UAV can be described by its equation of motion:

$$\begin{pmatrix} m\ddot{\boldsymbol{p}}_B \\ \Theta\dot{\boldsymbol{\omega}} \end{pmatrix} + \begin{pmatrix} \mathbf{0} \\ \boldsymbol{\omega} \times \Theta\boldsymbol{\omega} \end{pmatrix} + \begin{pmatrix} mg\boldsymbol{e}_z \\ \mathbf{0} \end{pmatrix} = \begin{pmatrix} \boldsymbol{f}_{\text{ext}} \\ \boldsymbol{\tau}_{\text{ext}} \end{pmatrix} + \boldsymbol{w}_{\text{act}}, \quad (1)$$

with the external forces $\boldsymbol{f}_{\text{ext}}$ and torques $\boldsymbol{\tau}_{\text{ext}}$. It is assumed that the origin of the frame $\mathcal{B}$ coincides with the center of gravity of the UAV. The actuation wrench $\boldsymbol{w}_{\text{act}}$ is related to the rotor angular velocities by $\boldsymbol{w}_{\text{act}} = \mathbf{J}\boldsymbol{\omega}^2_{\text{rotor}}$ with the constant mapping matrix $\mathbf{J}$, derived in [14].

B. Manipulator

The 1 DOF manipulator for screwing consists of a servo motor and a rigid transmission shaft extending beyond the rotors in the negative x axis of frame $\mathcal{B}$. The screw head is clamped into a screw holder similar to a socket wrench insert at the end of the shaft and is aligned with the rotation axis of the manipulator.

C. Architecture

The overall system architecture is shown in Fig. 3. A state machine manages the flight states based on contact and hole detection results. The reference pose given by the trajectory generator ξ_{ref} is adapted by an admittance filter to achieve a compliant behavior in the presence of external forces and kinematic constraints during the screwing operation and to generate the desired contact force. A 6-DOF pose controller

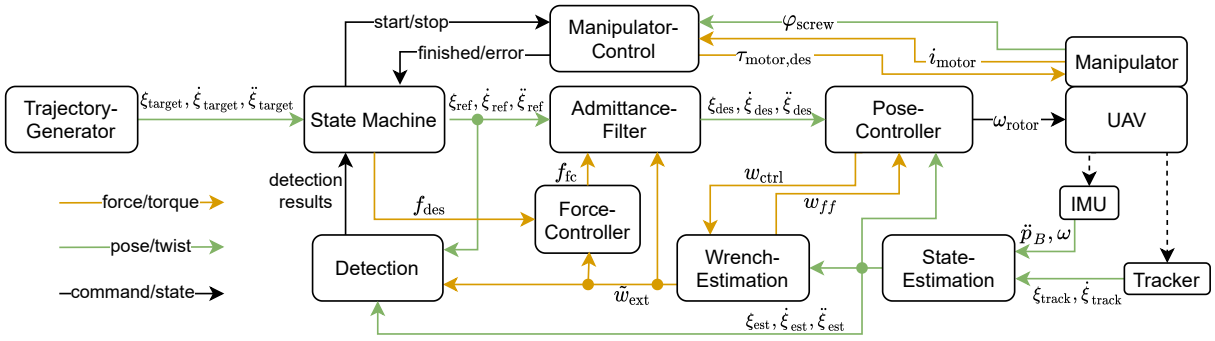

Fig. 3: Overall system architecture.

controls the angular velocities of the six rotor units. The current pose ξ_{est} is estimated fusing measurements from an IMU and an indoor localization system with an Extended Kalman Filter. The manipulator is controlled separately and interfaced via simple commands to start or stop the screwing process. The key components are described in detail in section IV.

IV. Control

A. Pose Control

The full pose of the UAV is controlled with a 6 DOF PID controller and additional feedback linearization. The control law is given by

$$\boldsymbol{f}_{\text{ctrl}} = \mathbf{K}_{Pt}\Delta\boldsymbol{p}_B + \mathbf{K}_{Dt}\Delta\dot{\boldsymbol{p}}_{\boldsymbol{B}} + \mathbf{K}_{It}\int_0^t \Delta\boldsymbol{p}_B \mathrm{d}t \tag{2}$$

for the position, and

$$\boldsymbol{\tau}_{\text{ctrl}} = \mathbf{K}_{Pq}\Delta\boldsymbol{q} + \mathbf{K}_{Dq}\Delta\boldsymbol{\omega} + \mathbf{K}_{Iq}\int_0^t \Delta\boldsymbol{q}\mathrm{d}t + \boldsymbol{\tau}_{\text{lin}} \tag{3}$$

for the orientation, with the linearization torque

$$\boldsymbol{\tau}_{lin} = \boldsymbol{\omega} \times \Theta\boldsymbol{\omega} \tag{4}$$

from (1). The diagonal matrices $K_{P\square}, K_{D\square}, K_{I\square} > 0$ represent the controller gain. The orientation error $\Delta\boldsymbol{q}$ is calculated from the orientation $\mathbf{R}_{WB}$ as

$$\Delta\boldsymbol{q} = \frac{1}{2}\left[\mathbf{R}_{WB,\text{des}}^{\top}\mathbf{R}_{WB} - \mathbf{R}_{WB}^{\top}\mathbf{R}_{WB,\text{des}}\right]_{\vee} \tag{5}$$

with the vee-operator $\vee$ that maps a skew symmetric matrix to the corresponding vector, thus making the error equivalent to an angle-axis-representation. The full wrench output to actuate the UAV is composed the following

$$\boldsymbol{w}_{\text{act}} = \boldsymbol{w}_{\text{ctrl}} - \boldsymbol{w}_{ff} \tag{6}$$

with the estimated external force as feed forward:

$$\boldsymbol{w}_{ff} = \begin{pmatrix} \tilde{\boldsymbol{f}}_{\text{ext}} \\ \mathbf{0} \end{pmatrix}. \tag{7}$$

B. Wrench Estimation

To estimate external forces and torques, a hybrid wrench estimator based on [1] is utilized. The estimated external wrench

$$\tilde{\boldsymbol{w}}_{\text{ext}} = \begin{pmatrix} \tilde{\boldsymbol{f}}_{\text{ext}} \\ \tilde{\boldsymbol{\tau}}_{\text{ext}} \end{pmatrix} \tag{8}$$

is calculated based on the actuation wrench $\boldsymbol{w}_{\text{act}}$, the linear acceleration $\ddot{\boldsymbol{p}}_B$ and angular momentum $\Theta\boldsymbol{\omega}$ of the UAV. The differential equation to obtain the external force estimate is given by

$$\tilde{\boldsymbol{f}}_{\text{ext}} = \mathbf{K}_f \cdot \int_0^t \left(-\tilde{\boldsymbol{f}}_{\text{ext}} - \boldsymbol{f}_{\text{act}} + m\ddot{\boldsymbol{p}}_B + mg\boldsymbol{e}_z\right) \mathrm{d}t' \tag{9}$$

whereas the external torque is estimated using

$$\tilde{\boldsymbol{\tau}}_{\text{ext}} = \mathbf{K}_{\tau} \cdot \left(\int_0^t \left[\boldsymbol{\omega} \times \Theta\boldsymbol{\omega} - \tilde{\boldsymbol{\tau}}_{\text{ext}} - \boldsymbol{\tau}_{\text{act}}\right] \mathrm{d}t' + \Theta\boldsymbol{\omega}\right) \tag{10}$$

with the filter gain matrices $\mathbf{K}_f, \mathbf{K}_{\tau} > 0$.

C. Admittance Filter

The admittance filter, applying additional compliance to the translational system behavior, is based on [1] and extended to allow controlling the contact force and the torque coupling to deal with the additional kinematic constraints during screwing.

The filter dynamics is described with

$$\mathbf{M}\Delta\ddot{\boldsymbol{p}}_f + \mathbf{B}\Delta\dot{\boldsymbol{p}}_f + \mathbf{C}\Delta p_f = \mathbf{P}\tilde{\boldsymbol{f}}_{\text{ext}} + \boldsymbol{f}_{\text{coup}} - \boldsymbol{f}_{fc}. \tag{11}$$

The mass $\mathbf{M}$, stiffness $\mathbf{C}$ and damping $\mathbf{B}$ can be chosen freely to create the desired system behavior. The desired position for the pose controller $\boldsymbol{p}_{\text{des}}$ is obtained from the filter dynamics by

$$\boldsymbol{p}_{\text{des}} = \boldsymbol{p}_{\text{ref}} - \Delta\boldsymbol{p}_f. \tag{12}$$

To achieve a high lateral position accuracy, a compliance to external forces is only applied perpendicular to the target surface. Assuming the world frame $\mathcal{W}$ and the target frame $\mathcal{H}$ to be parallel, the projection matrix $\mathbf{P}$ is given by $\mathbf{P} = diag([1\,0\,0])$. The coupling force $\boldsymbol{f}_{\text{coup}}$ and the force of the force controller $\boldsymbol{f}_{fc}$ are explained in the following. When the screw tip enters the hole, the lateral screw tip motion is constrained and lateral forces at the screw tip arise from

pose estimation errors and misalignment of the UAV w.r.t. the hole. Due to the reduced degree of freedom of the UAV, the position and orientation controller cannot act independently anymore. Thus, a decoupled 6-DOF pose control results in counteracting control forces and torques. By introducing wrench coupling, the UAV position becomes compliant to applied torques in order to allow the UAV position to align with the hole even without knowing the exact hole location. Assuming that the contact is established in x-direction w.r.t. the world frame and the screwdriver rotates about the x-axis of the UAV, the coupling force is calculated with the scaling factor $k_{coup} > 0$ as

$$\boldsymbol{f}_{\text{coup}} = k_{\text{coup}} \cdot \begin{bmatrix} 0 & 0 & 0 \\ 0 & 0 & -1 \\ -1 & 0 & 0 \end{bmatrix} \cdot \tilde{\boldsymbol{\tau}}_{\text{ext}}. \tag{13}$$

An external torque about the z-axis generates a force in y-direction to align the UAV horizontally, while a torque about the y-axis generates a force in z-direction to ensure the vertical alignment.

To control the contact force perpendicular to the target surface, a force controller applies the force $\boldsymbol{f}_{fc}$ to the admittance filter. Thereby, the desired position $\boldsymbol{p}_{\text{des}}$ is adjusted so that the position controller generates the desired contact force from the induced position error. The force controller is designed as a PID controller with the input force error $\Delta f = \mathbf{P}\left(\tilde{\boldsymbol{f}}_{\text{ext}} - \boldsymbol{f}_{\text{des}}\right)$. This approach thus ensures the desired contact force regardless of the actual implementation or model parameters of the position controller or admittance filter and takes full advantage of the fully actuated UAV structure.

D. Aerial Screwing State Machine

The strategy hereby proposed for the aerial screwing task is based on a cascaded finite state machine (FSM), illustrated in Fig. 4. In addition to what was previously presented in [6], the following strategy carefully breaks down the operations involved in the screwing process and presents a higher fidelity model to the real-world application, enabling a robust and repeatable outcome. The FSM receives a reference trajectory to the approximate location of the hole ξ_{ref} and renders the motion to accomplish the screwing task. During the state *Trajectory Tracking*, the vehicle is in free-flight and the trajectory to the approximate target location ξ_{target} is used as reference pose ξ_{target} for the admittance filter. When contact with the target surface is detected, the system transits to the *Contact* stage, where the force controller is activated and the desired contact force f_{des} is set. Subsequently, a *Search Pattern* state is enabled to move the screw tip systematically along the target surface to find the hole. During the search, the end-effector is kept perpendicular to the surface, which is assumed to be flat, and the vehicle moves parallel to the target surface. This state is maintained until the screw tip is detected to be in hole. The detection algorithm is described in section V. An additional state, *Hole Test*, verifies this condition: as the TCP is inside the hole, radial circular motion is imposed at the screw tip by slightly changing

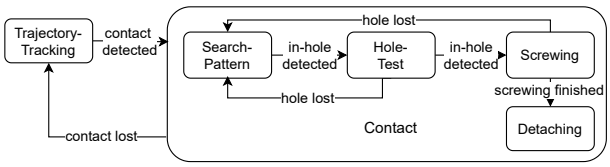

Fig. 4: Finite state machine architecture of the aerial screwing state machine.

the desired orientation of the UAV while keeping the body position constant. The verification is completed if the screw tip holds its position during the hole test. Subsequently, the *Screwing* process is started. In this state, the wrench coupling is activated and the torque-feeding actuator is started. An inner control loop runs on the manipulator, continuously evaluating the motor's current-torque output (see Section IV-E). When the screwing process terminates, the final state *Detaching* is initiated where a negative contact force is demanded on the admittance controller to disconnect the end-effector from the screw. After detachment, the TCP can move freely and therefore the *Trajectory Tracking* state is entered again, guiding the UAV to the home position.

E. Manipulator Control

The manipulator control is also based on a finite state machine architecture to represent the different stages throughout the screwing process. Starting in state *Idle*, a transition to state *Turning* is initiated by a start command from the FSM. In state *Turning* the motor operates in current control mode with limited speed. A desired maximum motor current proportional to the desired tightening torque is set. Thus, the desired motor current is only reached for a tightened screw. If the desired motor current is reached for a certain duration without any rotation of the motor, the screwing is stopped and a transition to state *Tightened* is initiated. The result is subsequently reported to the FSM and the manipulator control returns to state *Idle*.

V. Detection

To automate the screwing process and be able to use the proposed approach in the real world, both the detection of contact with the target surface and the hole location are of key importance. The detection algorithms rely, amongst other quantities, on the position of the TCP w.r.t. the world frame, expressed in the target frame ${}_H p_T$. For this section, estimated quantities are denoted with superscript $\tilde{\square}$, whereas desired quantities are denoted with superscript $\bar{\square}$.

A. Contact Detection

Contact established between the TCP and the target wall is the prerequisite and the trigger for activating the force controller on the aerial system. To improve robustness, the contact detection takes three different quantities into account:

1) Position error in the normal direction $\Delta p_{\perp}$:
   It is assumed that the contact surface prevents the TCP to reach its desired position. Thus, a position error in the direction normal to the contact surface (x-axis in

frame $\mathcal{H}$), while the UAV aims to move towards the wall ($_H\bar{v}_x < 0$), is an indicator for contact:

$$\Delta p_\perp = \begin{cases} \frac{{}_H\tilde{p}_{T,x} - {}_H\bar{p}_{T,x}}{\Delta p_0} & \text{if } {}_H\bar{v}_x < 0 \\ 0 & \text{else.} \end{cases} \tag{14}$$

with the normalization constant Δp_0.

2) Envelope of the TCP position in normal direction $\varepsilon_\perp$: During free flight, disturbances may cause the TCP to deviate from the desired position. At contact, the TCP x-position (in $\mathcal{H}$ frame) is aided by the presence of the wall itself, therefore the error in the normal direction is less subject to oscillation. The normalized position envelope is defined over the last N estimates of the TCP position as

$$\varepsilon_\perp = \frac{\varepsilon_{\perp,0} - [\max_N({}_H\tilde{p}_{T,x}) - \min_N({}_H\tilde{p}_{T,x})]}{\varepsilon_{\perp,0}} \tag{15}$$

with the reference envelope width $\varepsilon_{\perp,0}$.

3) Estimated contact force $f_\perp$:
As a third indicator for established contact, the normalized estimated contact force ${}_H\tilde{f}_x$ is considered with

$$f_\perp = \frac{{}_H\tilde{f}_x}{{}_H\bar{f}_x} \tag{16}$$

and normalized with the desired contact force ${}_H\bar{f}_x > 0$.

From these three indicators, a *confidence* value α_c is continuously computed from which the contact detection is inferred.

$$\alpha_c = \frac{c_1 \cdot \Delta p_\perp + c_2 \cdot \varepsilon_\perp + c_3 \cdot f_\perp}{\sum_{i=1}^{3} c_i} \tag{17}$$

$$\alpha_c > \alpha_{c,\text{thresh}} \qquad \textit{in contact} \tag{18}$$

with the empirically determined weight coefficients c_i and threshold $\alpha_{c,\text{thresh}}$.

B. Hole Detection

In a similar way, the hole detection algorithm accounts for two quantities:

1) Envelope of the TCP lateral motion $\varepsilon_\parallel$:
When the screw tip enters the hole, its lateral motion is blocked. This phenomenon is indicated by a reduced lateral motion of the TCP:

$$\varepsilon_\parallel = \frac{\sqrt{\Delta y^2 + \Delta z^2} - \varepsilon_{\parallel,0}}{\varepsilon_{\parallel,0}} \tag{19}$$

with $\Delta y = \left[\max_N({}_H\tilde{p}_y) - \min_N({}_H\tilde{p}_y)\right]$, and Δz comparably derived.

2) Estimated distance between the TCP and the wall d_w: The distance to the wall is defined as the difference of the estimated wall position to the momentary TCP position as

$$d_w = \frac{{}_H\tilde{p}_{wall,x} - {}_H\tilde{p}_{T,x}}{d_{w,0}} \tag{20}$$

with the normalization factor $d_{w,0}$. In addition, a decreased wall distance indicates that the screw has entered the hole. The wall position ${}_H\tilde{p}_{\text{wall},x}$ is estimated based on the TCP position during sliding on the target surface.

In the rare instance where the screw tip enters the hole at first contact, i.e. without sliding on the target surface, the above approach proves invalid as d_w cannot be computed. Therefore, a disambiguation for the overall in-hole confidence α_h is proposed:

$$\alpha_h = \begin{cases} \varepsilon_\parallel & \text{if } d_w \text{ is invalid} \\ \dfrac{c_4 \cdot \varepsilon_\parallel + c_5 \cdot d_w}{c_4 + c_5} & \text{else.} \end{cases} \tag{21}$$

If no valid wall distance is available, the hole detection is solely based on the lateral motion of the TCP. The in-hole detection results positive if contact is detected for at least 1 s, and the in-hole confidence is above a threshold $\alpha_h > \alpha_{h,\text{thresh}}$ for at least 1 s.

VI. Flight Experiments

A. Setup

The used UAV has a mass of 5.25 kg, its 15 inch rotors are alternately inclined by $\pm 20°$. The flight controller code runs on a ground computer and is described in more detail in [15]. To begin with, a plastic bolt and target hole with M20 thread are fabricated. Both the thread of the bolt and of the hole are machined. The surface area where the TCP can slide during the task consists of a 20 cm wide square, mounted on a 1-axis force sensor for ground-truth measurements. The friction coefficient between screw tip and slide area is approximately $\mu \approx 0.15$. The screw tip can enter the target hole with a maximum lateral displacement of about ± 1 mm. The screw holder is designed for a standard hexagon screw head, and it is connected to a Dynamixel XM540-W150 motor via a carbon fibre shaft.

During the *search pattern*, a star-shaped pattern of 6 cm diameter is followed to locate the hole. The pattern is designed to systematically cover an area around the assumed hole location. In contrast to a grid-shaped pattern, the star-shaped pattern causes a higher search density close to the assumed hole location. A precise following of the pattern is not necessary as its cause is to cover an area around the hole and not to define a distinct search path. In case of a higher uncertainty of the hole location, the search pattern can be scaled up to cover a wider area. During the *hole test* phase, an angular displacement of $2°$ is imparted on the UAV generating lateral forces of approx. 0.5 N at the TCP and verifying the in-hole presence. The peak torque reached when tightening the screw is approximately 0.5 Nm. All other relevant parameters used in flight experiments are specified in Tables I and II. The detection parameters are experimentally optimized throughout several calibration flights. The value for normalizing force ${}_H\bar{f}_x$ corresponds to the desired contact force of 2 N.

A HTC Vive[1] MoCap system is used to acquire the UAV's absolute pose. Additionally a Phidgets 1044[2] IMU is used

[1] www.vive.com

[2] https://www.phidgets.com/?&prodid=1038

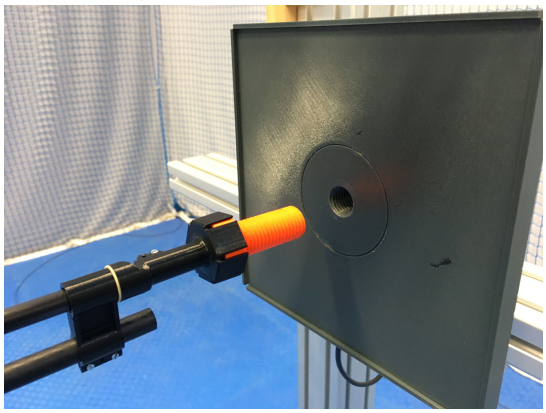

Fig. 5: Target surface with hole and end-effector with plastic screw.

TABLE I: Contact and hole detection parameters.

K_f K_τ	Δp_0	$\varepsilon_{\perp,0}$ $\varepsilon_{\parallel,0}$	${}_H\bar{f}_x$	$d_{w,0}$	$\alpha_{c,thresh}$ $\alpha_{h,thresh}$	$c_{1,2,4}$	c_3	c_5
$10 \cdot \mathbb{I}_{3\times3}$	2 cm	1 cm	2 N	5 mm	0.4	2	5	1

to improve the state estimation. The MoCap system can be replaced by visual odometry and an onboard distance sensor for outdoor experiments. To reduce communication latency between the UAV and the control software running on a ground computer, the UAV is connected with data cables to the ground computer. Power is supplied to the aerial system via a wired connection, to enable longer operational time.

B. Results & Discussion

To validate the proposed concept, 35 experiments are conducted. By observing the UAV's position in Fig. 6 (top plot), one can appreciate the different states of the finite state machine, highlighted by the colored areas. During screwing (between 48 s and 72 s), the x-position of the UAV slowly decreases as the screw tip immerses into the hole. In all following plots, the UAV position is shown in the $\mathcal{H}$ frame with an offset for better visibility.

The low-pass filtered forces and torques acting on the UAV body in flight are depicted in Fig. 6 (middle, bottom plots). The estimated and desired contact force, depicted in solid and dashed blue respectively, match very well throughout the whole experiment. The force sensor readings (green line) show deviations from the estimate during search pattern and hole test phase (between 39 s and 49 s), however they match well during the screwing phase. This behaviour is appointed to the presence of higher lateral forces, i.e. f_y and f_z, that come into play due to: 1) the friction between screw tip

TABLE II: Wrench estimator and admittance controller parameters.

$\mathbf{K}_f$, $\mathbf{K}_\tau$	**M**	**C**	**B**
$10 \cdot \mathbb{I}_{3\times3}$	$5 \cdot \mathbb{I}_{3\times3}$	*diag*([20, 20, 30])	*diag*([100, 100, 122])

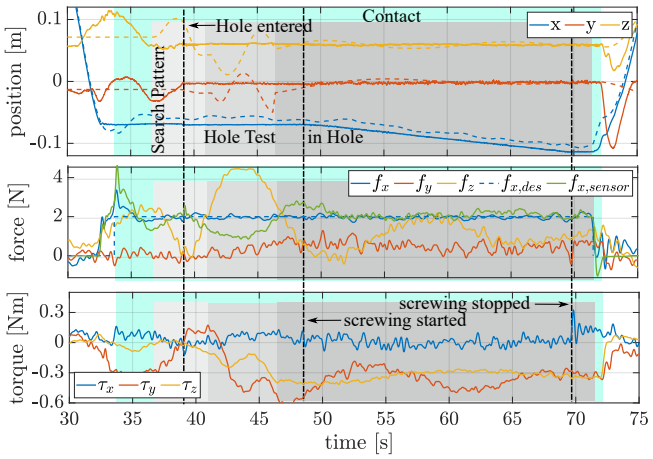

Fig. 6: Desired (dashed) and estimated position of the TCP (top), estimated forces (middle) and estimated torques (bottom), with highlighted states of the FSM.

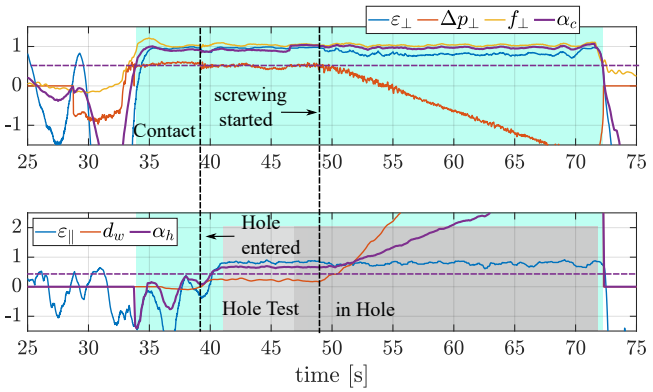

Fig. 7: Contact confidence (top) and hole confidence (bottom) during operation.

and target surface as the TCP slides along the target, 2) the data and power supply cables attached to the UAV, 3) the constraint reaction forces due to the hole test and 4) due to the misalignment of the UAV with the hole position. As the screw is completely screwed in, a peak in the x-torque with a subsequent plateau can be observed (blue line in bottom plot at 70 s stops). Reference measurements with a torque sensor show a peak tightening torque of 0.5 Nm. However, due to the low-pass filtering the peak torque shown in the plot is a little lower.

A key part of the proposed strategy is in the detection of the target and hole, prior to screwing. The transition from one state to another is based on the quantities described in Section V, and illustrated in Fig. 7. As the contact is established, all contact detection quantities show a simultaneous and significant increase in value. The same applies for the hole detection quantities as the screw enters the hole. As the screwing starts and the screw further immerses into hole, the position error $\Delta p_\perp$ is no longer considered for computing the contact confidence α_c, since it would deceive the hole detector to have missed the target surface. In the current

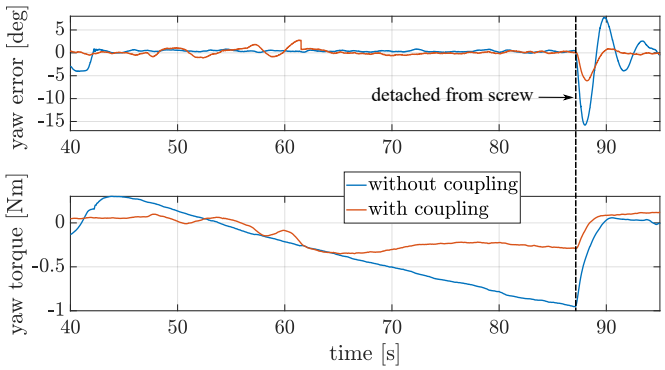

Fig. 8: Comparison of the yaw error and torque without (blue) and with torque coupling (red).

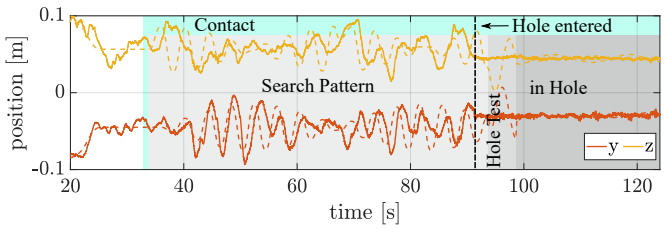

Fig. 9: Search pattern tracking for a flight with long search phase

approach, a motion capture system is used to ensure a good state estimation. Alternatively, a rangefinder could be used for estimating the wall distance and an onboard camera could be used to estimate the lateral movement of the screw tip relative to the target surface.

As the UAV detaches from the inserted screw, a motion of the TCP perpendicular to the contact surface causes the detector to detect a loss of contact (purple line in top plot at 72 s).

The effect of the proposed wrench coupling method is shown at an example in Fig. 8. Without wrench coupling, the orientation controller increases the yaw torque (i.e. about the z axis) to correct the yaw error that results from a lateral misalignment between the UAV and the hole. When the UAV detaches from the screw head and the contact constraints are released, this torque results in high yaw errors. Thanks to the wrench coupling, the yaw torque is limited as the UAV position is adjusted to align with the hole, significantly reducing the yaw error after detachment.

To illustrate the effectiveness of the search pattern, the TCP position of one sample experiment with a long search duration is shown in Fig. 9. The TCP follows the desired path qualitatively and with a slight delay. Considering the small search pattern size and the friction caused by the stick-slip characteristic, the TCP follows the desired path sufficiently well.

C. Robustness and Success Rate

To demonstrate the robustness of the hole detection algorithm, flight experiments are carried out where the TCP is purposely placed in the corner of the target surface, far apart

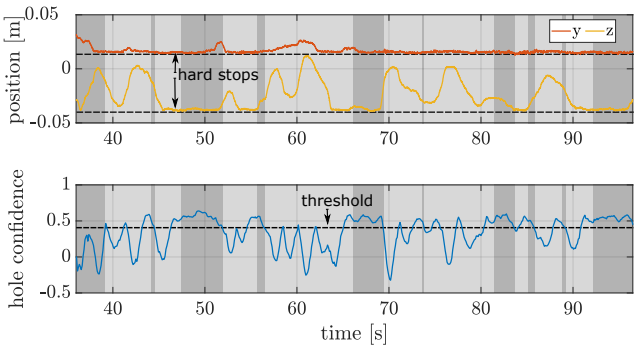

Fig. 10: Lateral TCP motion on $y-z$ axes (top plot) in a sample experiment where the TCP movement is purposely blocked by hard stops (dashed lines). The light gray areas indicate the *Search Pattern* states, while the dark gray areas indicate the *Hole Test* state. The bottom plot shows the hole confidence α_h and the corresponding threshold $\alpha_{h,\text{thresh}}$ being responsible for the transition between the two states.

from the real hole location. When in the corner, the TCP's lateral motion is limited in two directions by a mechanical border surrounding the target area, as depicted in Fig. 5. This hard stop blocks the TCP motion, causing an increase in the in-hole confidence α_h and therefore triggering the *Hole Test* state whenever $\alpha_h > \alpha_{h,\text{thresh}}$ applies for more than 1 s.

As the lateral motion in the remaining two directions is still possible, the hole test fails and the *Search Pattern* state is re-activated. Results from these tests are illustrated in Fig. 10. In the shown experiment, the longest hole test duration is 4.6*s* (from 47 s to 52 s) which is close to the maximum hole test time of 5.5*s*. As a falsely succeeded hole test is conceivable, the re-activation of the *Search Pattern* state is also possible from the *Screwing* state for additional robustness as shown in Fig. 4.

In order to demonstrate the robustness and repeatability of the whole framework, Fig. 11 shows a comparison of 30 successful flights. The time elapsed between initially entering the *Search Pattern* state and finally entering the *Hole Test* state is plotted against the true hole location within the search pattern.

The overall success rate for all 35 flights is 86%. A flight is considered as successful if the screw is completely screwed in, and the UAV reaches free flight again. Overall, 5 failed tests are experienced caused by flight instability. The reason for this behaviour can be appointed to weak state estimation experienced after many subsequent flights were carried out. This was however solved after rebooting the system and it is most likely independent from the presented methodology. A video of the performed flights is provided at https://youtu.be/jGJbtuPdbJg

VII. Conclusion

This paper presents an approach for automated aerial screwing staged out with contact detection, hole search, hole detection, screwing and detaching operations. A point of strength of our proposed strategy lies in the thoroughness

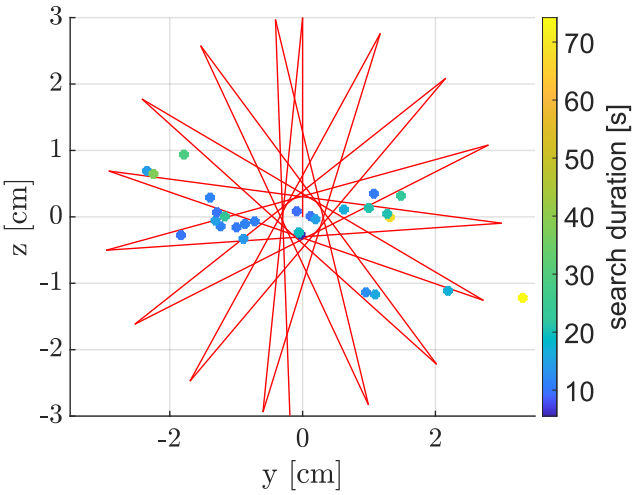

Fig. 11: True hole location relative to center of search pattern (expected hole location) and hole search duration. The desired search pattern is shown in red.

of the control architecture and its robustness to reject false positives. The pipeline has a success rate of 86% over 35 flights, and a median hole detection time of 9 s. Overall, our approach exploits the inherent features of fully-actuated platforms by applying 3D forces to the end-effector while maintaining a perpendicular orientation w.r.t. the target surface. In doing so, we avoid the use of external tools such as vision to aid detection or force sensing to guide the compliant behaviour while in contact.

Further work will investigate the integration of visual feedback in the form of visual inertial odometry to perform outdoor operations in full autonomy. Moreover, robustness against different sizes of screw, surface inclinations and surface textures will also be investigated.

REFERENCES

[1] M. Ryll, G. Muscio, F. Pierri, E. Cataldi, G. Antonelli, F. Caccavale, D. Bicego, and A. Franchi, "6d interaction control with aerial robots: The flying end-effector paradigm," *The International Journal of Robotics Research*, vol. 38, no. 9, pp. 1045–1062, 2019.

[2] D. Tzoumanikas, F. Graule, Q. Yan, D. Shah, M. Popovic, and S. Leutenegger, "Aerial manipulation using hybrid force and position nmpc applied to aerial writing," *arXiv preprint arXiv:2006.02116*, 2020.

[3] S. Hamaza, I. Georgilas, M. Fernandez, P. Sanchez, T. Richardson, G. Heredia, and A. Ollero, "Sensor installation and retrieval operations using an unmanned aerial manipulator," *IEEE Robotics and Automation Letters*, vol. 4, no. 3, pp. 2793–2800, 2019.

[4] M. Tognon, H. A. T. Chávez, E. Gasparin, Q. Sablé, D. Bicego, A. Mallet, M. Lany, G. Santi, B. Revaz, J. Cortés *et al.*, "A truly-redundant aerial manipulator system with application to push-and-slide inspection in industrial plants," *IEEE Robotics and Automation Letters*, vol. 4, no. 2, pp. 1846–1851, 2019.

[5] D. Kim and P. Y. Oh, "Human-drone interaction for aerially manipulated drilling using haptic feedback," in *2020 IEEE/RSJ International Conference on Intelligent Robots and Systems (IROS)*, 2020, pp. 9774–9780.

[6] C. Ding, L. Lu, C. Wang, and C. Ding, "Design, sensing, and control of a novel uav platform for aerial drilling and screwing," *IEEE Robotics and Automation Letters*, vol. 6, no. 2, pp. 3176–3183, 2021.

[7] A. Ollero, G. Heredia, A. Franchi, G. Antonelli, K. Kondak, A. Sanfeliu, A. Viguria, J. R. Martinez-de Dios, F. Pierri, J. Cortes, A. Santamaria-Navarro, M. A. Trujillo Soto, R. Balachandran, J. Andrade-Cetto, and A. Rodriguez, "The aeroarms project: Aerial robots with advanced manipulation capabilities for inspection and maintenance," *IEEE Robotics Automation Magazine*, vol. 25, no. 4, pp. 12–23, 2018.

[8] A. Lopez-Lora, P. J. Sanchez-Cuevas, A. Suárez, A. Garofano-Soldado, A. Ollero, and G. Heredia, "Mhyro: Modular hybrid robot for contact inspection and maintenance in oil & gas plants," in *2020 IEEE/RSJ International Conference on Intelligent Robots and Systems (IROS)*. IEEE, 2020, pp. 1268–1275.

[9] T. Ikeda, S. Yasui, M. Fujihara, K. Ohara, S. Ashizawa, A. Ichikawa, A. Okino, T. Oomichi, and T. Fukuda, "Wall contact by octo-rotor uav with one dof manipulator for bridge inspection," in *Proc. IEEE/RSJ International Conference on Intelligent Robots and Systems*, 2017, pp. 5122–5127.

[10] F. Forte, R. Naldi, A. Macchelli, and L. Marconi, "Impedance control of an aerial manipulator," in *2012 American Control Conference (ACC)*, 2012, pp. 3839–3844.

[11] K. Bodie, M. Brunner, M. Pantic, S. Walser, P. Pfändler, U. Angst, R. Siegwart, and J. Nieto, "Active interaction force control for contact-based inspection with a fully actuated aerial vehicle," *IEEE Transactions on Robotics*, vol. 37, no. 3, pp. 709–722, 2020.

[12] L. Peric, M. Brunner, K. Bodie, M. Tognon, and R. Siegwart, "Direct force and pose nmpc with multiple interaction modes for aerial push-and-slide operations," in *2021 IEEE International Conference on Robotics and Automation (ICRA)*. IEEE, 2021, pp. 131–137.

[13] M. Á. Trujillo, J. R. Martínez-de Dios, C. Martín, A. Viguria, and A. Ollero, "Novel aerial manipulator for accurate and robust industrial ndt contact inspection: A new tool for the oil and gas inspection industry," *Sensors*, vol. 19, no. 6, p. 1305, 2019.

[14] M. Schuster, D. Bernstein, C. Yao, K. Janscheck, and M. Beitelschmidt, "Comparison of design approaches of fully actuated aerial robots based on maximum wrench generation and minimum energy consumption," *IFAC-PapersOnLine*, vol. 52, no. 15, pp. 603–608, 2019, 8th IFAC Symposium on Mechatronic Systems MECHATRONICS 2019.

[15] M. Schuster, D. Bernstein, W. Reichert, K. Janschek, and M. Beitelschmidt, "Model-based development process of flight controllers for fully actuated multicopters by code export from simulink to ros," in *Fachtagung VDI MECHATRONIK 2022*, Darmstadt, Germany, 2022, pp. pp 53–60. [Online]. Available: https://tud.link/v3sq